Aerosol Science and Technology

ISSN: (Print) (Online) Journal homepage: https://www.tandfonline.com/loi/uast20

NanoSpot™ collector for aerosol sample collection for direct microscopy and spectroscopy analysis

Orthodoxia Zervaki, Braden Stump, Patricia Keady, Dionysios D. Dionysiou & Pramod Kulkarni

To cite this article: Orthodoxia Zervaki, Braden Stump, Patricia Keady, Dionysios D. Dionysiou & Pramod Kulkarni (2023) NanoSpot™ collector for aerosol sample collection for direct microscopy and spectroscopy analysis, Aerosol Science and Technology, 57:4, 342-354, DOI: 10.1080/02786826.2023.2167648

To link to this article: https://doi.org/10.1080/02786826.2023.2167648

AEROSOL SCIENCE AND TECHNOLOGY
2023, VOL. 57, NO. 4, 342–354
https://doi.org/10.1080/02786826.2023.2167648

NanoSpot™ collector for aerosol sample collection for direct microscopy and spectroscopy analysis

Orthodoxia Zervaki[a,b], Braden Stump[c], Patricia Keady[c], Dionysios D. Dionysiou[b], and Pramod Kulkarni[a]

[a]Centers for Disease Control and Prevention, National Institute for Occupational Safety and Health, Cincinnati, Ohio, USA; [b]Environmental Engineering and Science Program, Department of Chemical and Environmental Engineering (ChEE), University of Cincinnati, Cincinnati, Ohio, USA; [c]Aerosol Devices Inc, Fort Collins, Colorado, USA

ABSTRACT

We describe design and characterization of an aerosol NanoSpot™ collector, designed for collection of airborne particles on a microscopy substrate for direct electron and optical microscopy, and laser spectroscopy analysis. The collector implements a water-based, laminar-flow, condensation growth technique, followed by impaction onto an optical/electron microscopy substrate or a transmission electron microscopy grid for direct analysis. The compact design employs three parallel growth tubes allowing a sampling flow rate of 1.2 L min^{-1}. Each growth tube consists of three-temperature regions, for controlling the vapor saturation profile and exit dew point. Following the droplet growth, the three streams merge into one flow and a converging nozzle enhances focusing of grown droplets into a tight beam, prior to their final impaction on the warm surface of the collection substrate. Experiments were conducted for the acquisition of the size-dependent collection efficiency and the aerosol concentration effect on the NanoSpot™ collector. Particles as small as 7 nm were activated and collected on the electron microscopy stub. The collected particle samples were analyzed using electron microscopy and Raman spectroscopy for the acquisition of the particle spatial distribution, the spot sample uniformity, and the analyte concentration. A spot deposit of approximately 0.7-mm diameter is formed for particles over a broad particle diameter range, for effective coupling with microscopic and spectroscopic analysis. Finally, the NanoSpot™ collector's analytical measurement sensitivity for laser Raman analysis and counting statistics for fiber count measurement using optical microscopy were calculated and were compared with those of the conventional aerosol sampling methods.

ARTICLE HISTORY
Received 20 October 2022
Accepted 25 December 2022

EDITOR
Jingkun Jiang

1. Introduction

Understanding physical structure and morphology as well as chemical constituents of aerosol particles is of critical importance to understand their health effects upon inhalation exposure in atmospheric and occupational environments. Filter collection of aerosol particles, followed by their laboratory analysis using analytical methods is the most commonly used approach for determining the particles' chemical constituents (Raynor et al. 2011). However, careful sample pretreatment involving chemical or thermal manipulation of the filter media and the collected particles, and transfer of particles from the filter media to a suitable solvent or substrates is often required for speciation and quantitation of the target analytes. This sample pretreatment can introduce sample damage, matrix effects, or analyte loss. Moreover, the filter sample preparation steps are time- and labor-intensive, adding to longer turnaround times. In addition, filter collection of particle samples presents several challenges for electron microscopy (EM) analysis, which include: (i) transfer of particles to EM-compatible substrates without altering particle morphology, and (ii) poor sampling statistics associated with low spatial density of particles on the filter surface.

Collection of particles onto a spot smaller than 1 mm in diameter—referred to as "spot sample" hereafter—has been proven very useful to lower analytical detection limits, when coupled with laser spectroscopic analysis such as Raman (Zheng et al. 2018; Wei

CONTACT Pramod Kulkarni PSKulkarni@cdc.gov Centers for Disease Control and Prevention, National Institute for Occupational Safety and Health, 1090 Tusculum Ave, Cincinnati, OH 45226, USA.

Supplemental data for this article can be accessed online at https://doi.org/10.1080/02786826.2023.2167648.

et al. 2022) or infrared spectroscopy (Wei et al. 2017, 2020). The limit of detection (LOD) of respirable crystalline silica (RCS) quartz reported by Zheng et al. (2018) was in the range of 8 to 55 ng using the Sequential Spot Sampler™, which was orders of magnitude lower compared to that for total filter collection (estimated at 5 µg per sample for RCS quartz using standardized X-ray diffraction (XRD) and Infrared (IR) analysis). Similar enhancements in sensitivity were demonstrated by Wei et al. (2017) for infrared absorption analysis using quantum cascade lasers. However, current devices used for collection of spot samples (i.e., Sequential Spot Sampler) are relatively bulky and are not appropriate for portable or field monitoring applications, such as sampling in workplace atmospheres. Moreover, the Sequential Spot Sampler is designed for sequential collection in a well plate either as a dry spot or as liquid suspensions and is not suitable for direct microscopy analysis without additional sample preparation steps.

Here we describe the design and characterization of a compact, lightweight, hand-portable NanoSpot Collector (NSC) for collection of particles as spot samples directly onto EM—or laser spectroscopy—compatible substrates. The compact particle collector implements the condensational growth technique through water vapor diffusion in laminar-based aerosol flow. Detailed characterization of the performance of this spot collector is presented.

2. Design of NanoSpot™ Collector (NSC)

The operating principle of the NanoSpot Collector (NSC) is similar to that of the Sequential Spot Sampler (Series 110 A, Aerosol Devices Inc., Fort Collins, CO, USA). The NSC was designed for aerosol collection in field applications such as sampling in workplace atmospheres. Compact size, low weight, and hand-portability are essential features for such field applications. Moreover, it is also desirable to maintain high sampling flow rates to allow microscopy analysis with acceptable uncertainty. The NSC was designed to address these needs, while maintaining similar sampling flow rate as the Sequential Spot Sampler. The key difference is that the NSC uses three shorter parallel growth tubes, each designed for laminar flow condensational growth in a super-saturated water vapor, which significantly minimizes the size and the weight of the collector. The size of the NSC is 250 × 280 × 290 mm (H × W × D) and it weighs approximately 4 kg (Figure 1a). Each growth tube consists of three sections with a predetermined temperature profile that controls the supersaturation profile along the tube axis as the aerosol enters and exits each of the three growth tubes. Following the scheme proposed by Hering,

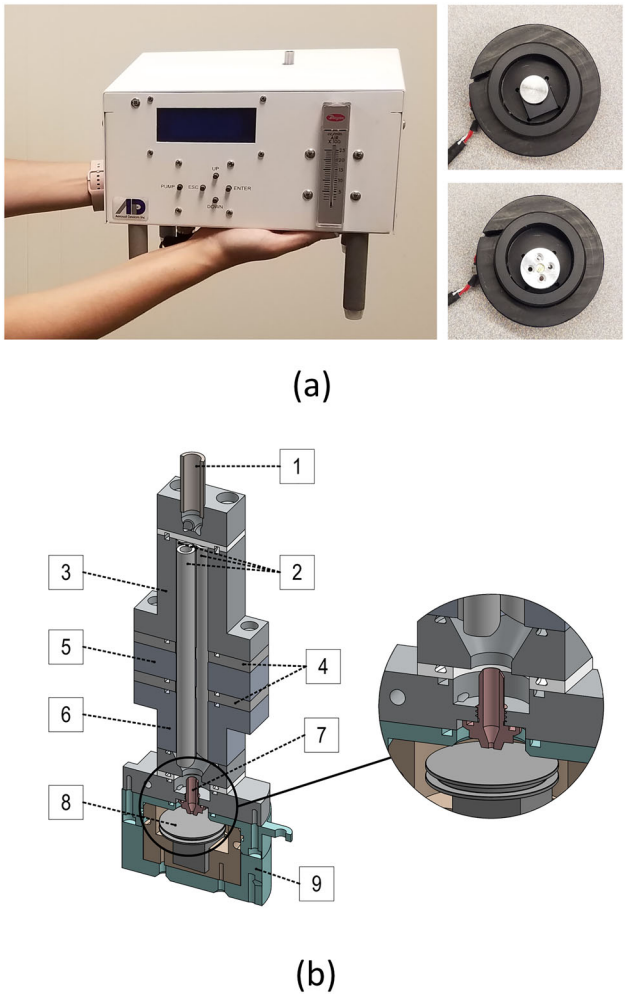

Figure 1. (a) Image of the NanoSpot collector and the sample heater chamber with an SEM stub and a TEM grid holder. (b) Cross sectional view of aerosol sampling, three-stage, moderated, triple growth tube, and collection section of prototype NanoSpot collector. (1) Aerosol inlet, (2) Rolled, filter-media wicks, (3) "Conditioner" section, (4) Insulators, (5)" Initiator" section, (6) "Moderator" section, (7) Focusing nozzle, (8) SEM stub and (9) Sample heater chamber.

Spielman, and Lewis (2014), the aerosol flow is first exposed to a cold section (T = 5 °C), followed by a hot section (T = 40–45 °C), where the water vapor diffusion rate is higher than the heat dissipation rate promoting the condensational growth. In the third section, lower temperature (T = 12 °C) is maintained to reduce the dew point of the aerosol flow when it exits the growth tube.

Figure 1b shows the configuration of the growth tubes in the NSC. The aerosol inlet is located at the top of the instrument where particle-laden stream at a total sample flowrate of 1.2 L min^{-1} enters though a stainless-steel tube with an ID of 6.9 mm. The flow is then divided through a three-way flow splitter into three flows at an 150° angle with the longitudinal axis of the growth tube, and then enters the three parallel growth tubes (each with 7 mm ID). The walls of the

growth tubes are made of rolled Durapore® membrane, that are kept fully saturated using periodic water injection. The rolled membranes have a thickness of 1.25 mm and an ID of 4.5 mm. First, the aerosol stream is introduced into the "conditioner" stage. The length of the conditioner region is approximately 45.5 mm, and the temperature is set to 5 °C (T_{cond}). During this stage the aerosol stream becomes fully saturated at the established temperature. Downstream of the "conditioner" stage is the "initiator" region (approximately 12.2 mm long), with a temperature set at 40–45 °C (T_{ini}). The abundance of water vapor that diffuses from the warm wetted walls, induces supersaturation in the flow path, leading to nuclei activation and condensational growth of the particle-enclosed droplets. The growth of the droplets continues in the "moderator" stage, which has a length of approximately 26.2 mm and the temperature is controlled at 12 °C (T_{mod}). This lower temperature leads to the lowering of exit dew point of the sample flow. The three stages are separated with insulators to reduce heat transfer between the stages.

Following the final stage, the three streams from each growth tube merge into one flow, and a 1-mm diameter converging nozzle enhances the focusing of the grown droplets into a single particle beam prior to the final impaction of droplets onto the substrate (heated SEM stub or a TEM grid; Figure 1a). The nozzle-to-plate distance is 2.6 mm. The collection substrate is heated to 35 °C, to allow evaporation of the collected water and acquisition of a dried spot sample. Temperature of the focusing nozzle is maintained at 25 °C to prevent water vapor condensation on the walls. Nozzle temperature does not appear to have any impact on the droplet growth.

Two thermoelectric coolers (TECs) were used to control the temperature of the "conditioner" and "moderator" sections. Miniature resistive heaters were used to heat the "initiator" stage, the nozzle, and the collection substrate.

A water injection pump adds approximately 15 μL of water per injection at the initiator stage. A water extraction pump removes approximately 0.1 L min^{-1} of condensed water and air at the base of the growth tubes, while the air sampling pump is operating.

3. Numerical simulation of particle growth in NSC

Numerical simulations were conducted to obtain axial and radial distribution of saturation ratio in a single growth tube. Navier-Stokes equations involving coupled momentum-, mass-, and heat-transfer equations, governing the axial and radial flow field, water vapor distribution, and temperature distribution in the growth tube (conditioner, initiator, and moderator) were obtained using the finite elements method (COMSOL Multiphysics®; v 5.6). A 2 D axisymmetric geometry was used. Local vapor pressure profile and temperature distributions were used to obtain local saturation ratio (S_R), which was defined as (Hinds 1999; Seinfeld and Pandis 2012):

$$S_R = \frac{P_i}{P_0} \tag{1}$$

where P_i is the local partial vapor pressure in a system and P_0 is the equilibrium vapor pressure at a given temperature of the system. Momentum transfer was described by the following equations:

$$\rho\left(\frac{\partial u}{\partial t} + u\nabla u\right) = -\nabla p + \mu\nabla^2 u + \frac{1}{3}\mu\nabla(\nabla u) + \rho g \tag{2}$$

$$\nabla(\rho u) = 0 \tag{3}$$

where ρ denotes the air density (calculated from the ideal gas law equation), u is the air velocity vector, p is the pressure, μ is the fluid dynamic viscosity, g is the gravitational acceleration constant, and t is the time. Approximately 765×10^3 triangular and quad mesh elements were selected. An atmospheric pressure boundary condition was used at the inlet of conditioner, while an average air flow velocity of 0.42 m s^{-1}, corresponding to flow in each tube, was used as the outlet boundary condition. Heat and mass transfer in the growth tube were described by the following equations (Bird, Stewart, and Lightfoot 2007):

$$\rho C_p u \cdot \nabla T + \nabla \cdot q = Q, \text{ where } q = -k\nabla T \tag{4}$$

$$u \cdot \nabla c_i + \nabla \cdot j_i = R_i, \text{ where } j_i = -D_i \nabla c_i \tag{5}$$

where C_p is the heat capacity of the air at constant pressure, k is the air thermal conductivity, Q is the heat source, and q is the heat flux vector; c_i, j_i, R_i and D_i are the molar concentration, the mass flux vector, the mass source, and the diffusivity of species i. The growth tube wall was held at fixed temperature. The inflow temperature was set at 20 °C, with a relative humidity of 50%. The vapor concentration on the tube wall was assumed equal to the local saturation concentration at the respective wall temperature. The values and expressions of the air and water vapor properties are shown in Table S1 in SI.

The Kelvin diameter ($D_{p,\ Kelvin}$), the threshold particle diameter that can neither grow nor evaporate, was described by (Hinds 1999; Seinfeld and Pandis 2012):

$$D_{p,\,Kelvin} = \frac{4\sigma MW_w}{\rho RTlnS_R} \tag{6}$$

where σ, MW and ρ denote to the surface tension, the molecular weight and the density of the droplet, R is the universal gas constant, and T and S_R are the local temperature and saturation ratio. At T_{ini}= 40 and 45 °C, S_R= 1.6 and 1.8, and at the bulk temperature of 290 and 291 K, the $D_{p,\ Kelvin}$ was estimated to be 4.7 and 3.7 nm, respectively. Thus, all particles with a diameter greater than 5 nm (T_{ini}=40 °C) or 4 nm (T_{ini}=45 °C) are expected to be activated for droplet growth.

Using the flow field, distribution of saturation ratio and temperature in the growth tube, particle trajectories were obtained by solving the ordinary differential equations that account for local flow field, local saturation ratio and the resulting droplet growth dynamics. The built-in particle tracing module in COMSOL was used for these calculations. The rate of droplet growth ($\frac{dd_p}{dt}$; Seinfeld and Pandis 2012) was given by:

$$d_p\frac{dd_p}{dt} = \frac{S_R - \exp(4MW_w\sigma/RT\rho d_p)}{(\rho RT/4P_0D_v^{'}MW_w) + (\Delta H_v\rho/4k_a^{'}T)((\Delta H_vMW_w/RT)-1)} \tag{7}$$

$$D_v^{'} = \frac{D_v}{\left(1+(2D_v/a_cd_p)(2\pi MW_w/RT)^{1/2}\right)} \tag{8}$$

$$k_a^{'} = \frac{k_a}{\left(1+(2k_a/a_T d_p\rho_{air}c_p)(2\pi MW_{air}/RT)^{1/2}\right)} \tag{9}$$

The notations and values or expressions of the parameters shown in the above equations are listed in Table S1 in SI. The time-dependent particle's position and velocity were then given by:

$$v = \frac{dq}{dt} \tag{10}$$

$$\sum F = m_p\frac{dv}{dt} \tag{11}$$

where q, v, and m_p denote the particle's position, velocity, and mass, respectively. The sum of external forces acting on the particle is denoted by $\sum F$. The drag force (F_D) on the particle was given by (Clift, Grace, and Weber 1978):

$$F_D = \frac{1}{\tau_p S}m_p(v - v_{fluid}) \ \text{ where } \ \tau_p = \frac{\rho_p {d_p}^2}{18\ \mu} \tag{12}$$

$$S = 1 + \frac{\Lambda}{d_p}\left(C_1 + C_2\ \exp\left(-\frac{C_3 d_p}{\Lambda}\right)\right) \tag{13}$$

where v_{fluid} is the velocity of the fluid, τ_p is the particle velocity response time, S is the slip correction factor, ρ_p is the particle density, Λ is the mean free path and Δt the time step taken by the numerical solver. A time step of 10^{-5} s was used to obtain adequately space- and time-resolved particle trajectories. The Cunningham-Milliken-Davies slip correction parameters, C_1, C_2 and C_3, were assigned with values of 2.514, 0.8 and 0.55, respectively (Davies 1945; Allen and Raabe 1982). Brownian force was neglected due to the rapid droplet growth to larger sizes at which the Brownian diffusion was negligible.

A 20 nm diameter seed particle, with a density of 1 g cm^{-1}, was released at a z-coordinate where droplet growth initiated ($dd_p/dt > 0$), and at r = 0 (centerline) and r/R = 0.5 (at t = 0 s).

For the downstream nozzle before impaction, the impactor cutoff particle size was calculated using the Stokes number, with nozzle diameter as the characteristic dimension:

$$Stk = \frac{\rho_p {d_p}^2 UC_c}{9\mu D_j} \tag{14}$$

where U is the air velocity, C_c is the Cunningham slip correction factor, and D_j is the nozzle diameter. The impaction nozzle had a cutoff d_{p50} (corresponding to $\sqrt{Stk}$=0.47) of about 1100 nm at the operating conditions used in the NSC. Simulations were also conducted to estimate particle losses through the impaction nozzle. The details of these loss calculations are presented in section S2 in SI.

4. Experimental methods

Experiments were designed and conducted for the evaluation of the NSC based on the following key variables: (i) The particle diameter dependent collection efficiency, (ii) the number concentration dependent collection efficiency, (iii) the deposition spot diameter on the collection substrate, (iv) the spot sample deposit uniformity, and (v) the comparison of analytical measurement sensitivity of NSC with other collection methods. The collection efficiency measurement scheme used in this study was similar to that used by Eiguren Fernandez, Lewis, and Hering (2014), and was based on the particle transmission efficiency measurements.

The experimental set up used for the evaluation of the collection efficiency of the NSC, is shown in Figure 2. A medical nebulizer (Salter 8900 Series Disposable Small Volume Jet Nebulizer; Salter Labs, Arvin, CA, USA) was used for the generation of the aerosols. Liquid solutions of sodium chloride (soluble) and suspensions of respirable crystalline silica (insoluble) were used. A diffusion dryer (model 3062, TSI Inc., Shoreview, MN,

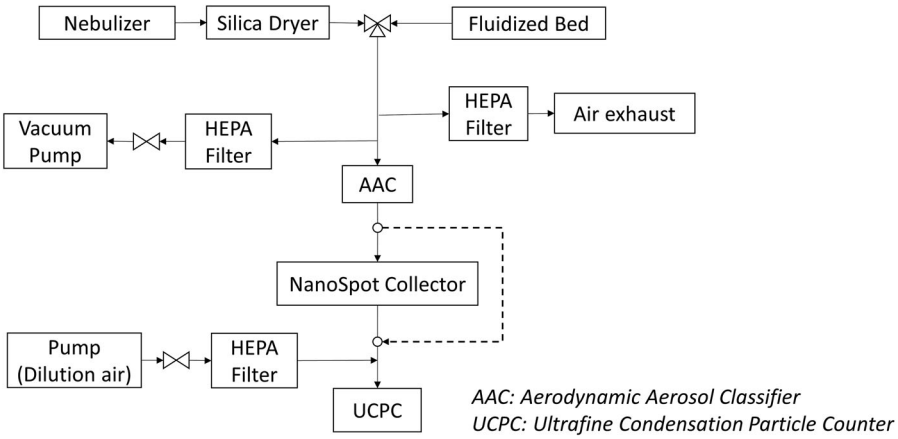

Figure 2. Schematic diagram of the experimental set-up for the characterization of the NanoSpot collector. Same UCPC was used to measure inlet and outlet concentrations for transmission efficiency measurement.

USA) was used downstream of the nebulizer for removal of water vapor. Crystalline silica aerosol was also generated from a dry powder using a fluidized bed aerosol generator (model 3400 A, TSI Inc., Shoreview, MN, USA). The aerosol exiting the fluidized bed generator had a relative humidity of 60%. The Aerodynamic Aerosol Classifier (AAC; Cambustion Ltd, Cambridge, United Kingdom) was used to obtain classified near-monodisperse (in aerodynamic size) test aerosol above 25 nm diameter, while an Electrostatic Classifier (model 3080; TSI Inc., Shoreview, MN, USA) and a Nano-Differential Mobility Analyzer (model 3085; TSI Inc., Shoreview, MN, USA) were used to obtain smaller particle sizes. Aerosols generated by the nebulizer, were classified through the nano-DMA and the AAC, while for the crystalline silica particles generated by the fluidized bed, only the AAC was used. During the collection efficiency evaluation, a total flowrate of 1.2 L min^{-1} was introduced into the NSC. The outlet of the collector was connected to an Ultrafine Condensation Particle Counter (model UCPC 3776; TSI Inc., Shoreview, MN, USA) to measure the number of particles that were transmitted throughout the collector. The UCPC required a total flowrate of 1.5 L min^{-1}; thus, filtered, dilution air was added as make-up air to the aerosol stream exiting the collector. The same UCPC with the make-up air was also connected at the inlet of the NSC for measuring the total aerosol concentration upstream of the collector. The collection efficiency was defined as,

$$\eta_c = 1 - \frac{N_{in} - N_{out}}{N_{in}} \quad (15)$$

where N_{in} (cm^{-3}) corresponds to the total number concentration measured by the particle counter before the NSC inlet and N_{out} (cm^{-3}) corresponds to the number concentration measured by the particle counter at the outlet of the NSC. The dilution by the make-up air is accounted for by being consistently applied to both number concentration measurements.

The collection efficiencies for different particle diameters and at different number concentrations were measured. Firstly, the effect of particle diameter on the NSC performance was compared at two initiator temperatures, 40 or 45 °C. Three temperature combinations for the initiator and the moderator were tested for the number concentration effect: 40 and 12 °C, 45 and 12 °C, and 45 and 25 °C.

Polystyrene latex (PSL) nano and micro-spheres (Thermo Fisher Scientific, Waltham MA, USA) were used for studying the characteristics of the spot sample collected on the substrate. A broad size range of polystyrene spheres (20, 100, 700 and 1900 nm) was generated using the medical nebulizer and the diffusion dryer, for examining potential particle size effects on the diameter of the spot sample. A Scanning Electron Microscopy (SEM) stub was positioned in the sample heater chamber of the collector, and an aluminum backed carbon tape (Ted Pella Inc., Redding CA, US) was placed on the surface of the stub, for the acquisition of superior SEM (Phenom XL Desktop SEM, Thermo Fisher Scientific, Waltham MA, USA) images on a smooth surface with minimum uneven illumination effects. The ImageJ software (Schneider, Rasband, and Eliceiri 2012) was implemented for measuring the projected area of the accumulated particles depicted on the SEM images. The calculated spot deposit diameter (D_{90}) corresponds to the diameter of the circle that contains 90% of the total projected area of the collected particles in the spot sample.

Test aerosols for Raman measurement were obtained using aerosolization of dry crystalline silica powder (Min-U-Sil@5; US Silica, Katy TX, USA) in a fluidized bed generator. The SEM stub's surface was cleaned with isopropyl alcohol before mounting into the sample chamber of the collector. During the

particle collection, a piezo balance dust monitor (model 3520; Kanomax, Andover NJ, USA) was used to simultaneously quantify the aerosol mass concentration entering the NSC. The nominal analyte mass (m_p), based on the inlet aerosol concentration entering the NSC was calculated as follows:

$$m_p = C_i \; t_c \; Q \tag{16}$$

where C_i is the mass concentration measured by the dust monitor (mg cm^{-3}), t_c is the collection time (min) and Q is the NSC flowrate (equal to 1.2 L min^{-1}).

For the Raman signal intensity acquisition, the portable i-Raman Spectrometer (i-Raman®; B&W Tek, Newark, DE, USA) was implemented. The maximum laser power and the laser spot diameter incident on the sample was 420 mW, and about 105 micrometers, respectively. The excitation wavelength was at 785 nm. An integration time of 30 s was used for this study. The characteristic peak for crystalline silica was observed at a Raman shift of 465 cm^{-1} for α-quartz. The Raman calibration curves were constructed by using the area below the characteristic peaks and the particulate mass collected on the SEM stub.

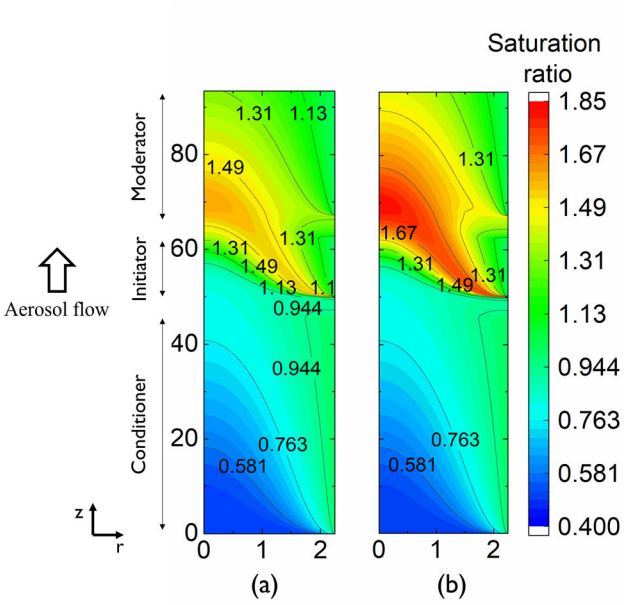

Figure 3. Saturation ratio profiles calculated for each growth tube of the NanoSpot collector, for T_{ini} equal to (a) 40 °C and (b) 45 °C. The z-coordinate corresponds to the centerline of the growth tube. The r- and z-coordinates represent distances in units of millimeters. The inlet of the growth tube is located at z = 0.

5. Results and discussion

5.1. Saturation ratio and droplet growth calculations

Axial and radial distributions of saturation ratio in the growth tube obtained from the numerical simulations are shown in Figure 3 for an initiator temperature of 40 and 45 °C. The maximum saturation ratio is expected to be reached along the centerline of the tube and approaches the values of 1.6 and 1.8 for an initiator temperature of 40 and 45 °C, respectively. Based on calculations, all particles with a diameter greater than 5 nm (T_{ini} = 40 °C) or 4 nm (T_{ini} = 45 °C) are expected to grow. Supersaturation is initiated toward the end of growth tube and reaches peak in the moderator.

The growth dynamics of a 20-nm diameter particle released at r = 0 and r/R = 0.5, at a z-coordinate where droplet growth initiated, are shown in Figure 4. Droplets grow to a diameter > 3.9 µm. The final droplet diameter depends on the radial position of the particle inside the growth tube. The particles/droplets located closer to the growth tube walls are expected to grow in bigger sizes than the ones located closer to the central axis (Hering, Spielman, and Lewis 2014). Moreover, the higher the initiator temperature, the greater the size of the droplet exiting the growth tubes. Droplet growth can also be expected downstream of the nozzle, assuming rapid expansion through the converging nozzle

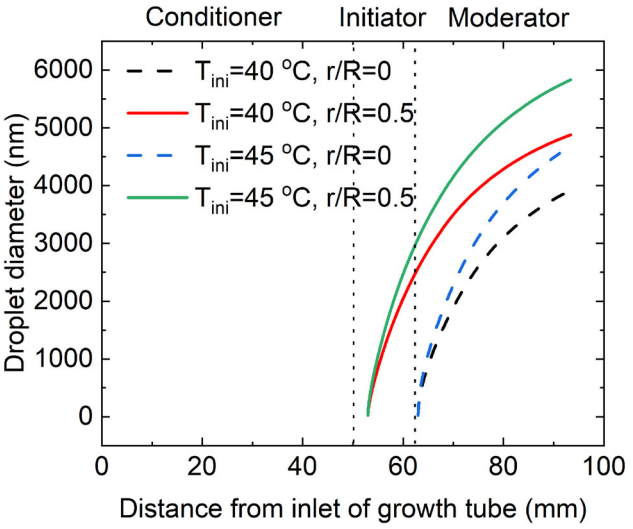

Figure 4. Calculated droplet diameter as a function of the axial distance downstream of the growth tube inlet for a 20-nm diameter particle released at z-coordinate where droplet growth started.

(Aitken 1888). Based on the designed d_{p50} of the impaction nozzle, all droplets larger than about a 1.1 µm diameter will be collected in the NSC.

The particle losses across the NSC due to inertial deposition, flow splitting at the inlet, and flow merging at the outlet of the growth tubes were also calculated and are presented in Figure S1 in SI. Inertial deposition was found to be independent of the initial particle

diameter and totaled at approximately 13% (Figure S1 in SI), of which 5% occurred at the inlet walls of the NSC, another 5% at the interior of the growth tube walls and approximately 3% at the converging nozzle. The size-independent particle losses inside the NSC are rather insignificant, thus were excluded in the measured collection efficiency. Quantification of a collected analyte mass can be achieved through mass calibration curves obtained by spectroscopic analysis, that only considers the actual airborne particulate mass at the inlet of the collector.

5.2. Droplet growth and collection efficiency in the NSC

The particle size-dependent collection efficiency of the NSC prototype, as concluded from the particle transmission efficiency measurements, was experimentally measured, and is shown in Figure 5, for two different aerosol types, sodium chloride and crystalline silica. Collection efficiency was greater than 90% for NaCl particle diameters down to 8 nm, at an initiator temperature of 40 and 45 °C. When crystalline silica particles are generated through dry silica powder, the collection efficiency starts decreasing at 25 nm aerodynamic diameter. For silica particles generated through the medical nebulizer, nearly complete collection has been attained for particle mobility diameters down to 7 nm, as shown in the inset plot of Figure 5. The initiator temperature hardly affected the collection efficiency of the silica particles. Generally, collection efficiency greater than 90% can be achieved for all types of aerosols, particle diameters, and NSC configuration. The average efficiency, based on number counts, was 95% NaCl and 93% for silica aerosols. Collection efficiency for the smallest particle diameter of 7 nm that was tested experimentally, was about 93%.

The particulate mass collected on the substrate is a function of the activation efficiency of the particles and the particle loss inside the collector and plumbing system. Diffusional losses, inertial deposition, droplet bouncing or splattering on the collection substrate, poor activation efficiency, and insufficient growth can contribute to reduced collection. Based on the particle size range studied here, gravitational deposition at the interior of the vertical growth tubes is assumed to be negligible (Brockmann 2011). The diffusional transport loss of nanoparticles in the growth tubes was calculated and is shown in Figure S2 in SI. Less than 10% of the particles with a diameter equal or greater than 6 nm are expected to be deposited on the interior of the growth tube walls due to diffusion. Droplet splatter upon impaction can contribute to artifacts and it may be desirable to use lower nozzle jet velocity. However, collection efficiency

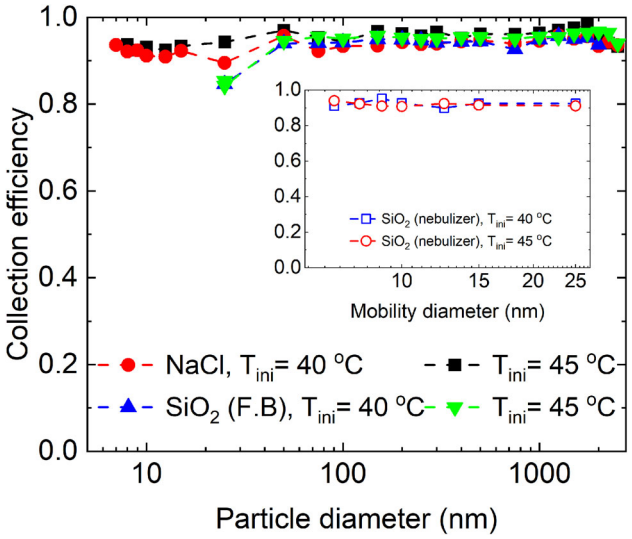

Figure 5. Collection efficiency measured for the NanoSpot collector using sodium chloride and crystalline silica aerosol at two different initiator temperatures.

of NSC measured in our study was >90% at all seed particle sizes studied, suggesting that the particle loss from droplet splatter or particle bounce may not be significant. Finally, the aerosol flowrate implemented in the NSC along with the growth tube scheme configuration used in the NSC has been successfully used earlier for droplet growth (Hering, Spielman, and Lewis 2014; Hering et al. 2019) and collection (Eiguren Fernandez, Lewis, and Hering 2014). Thus, effective activation, growth and collection is anticipated in the NSC, without any droplet bouncing and/or splashing on the collection substrate.

5.3. Effect of aerosol number concentration on collection efficiency

Figure 6 shows the effect of number concentration of 100 nm particles on the overall collection efficiency. The optimum collection efficiency was attained at the 45 °C initiator temperature, as anticipated. When the moderator temperature and dew point of the flow exiting the nozzle is increased from 12 to 25 °C, the collection efficiency does not seem to be affected significantly; thus, the moderator temperature does not seem to have a significant impact on collection efficiency and no appreciable evaporation loss downstream of the converging nozzle was observed.

At the lower initiator-moderator temperatures 40 and 12 °C, the collection efficiency starts decreasing above an aerosol number concentration of $8 \times 10^4\,cm^{-3}$, when it drops below 90%. At increased initiator temperature of 45 °C, the collection efficiency starts to decrease above a number concentration of approximately $3 \times 10^5\,cm^{-3}$. When the moderator

temperature is set at 25 °C, higher relative humidity of the droplet-laden stream is rendered, while minimum collection performance improvement is observed, since the collection efficiency starts dropping below 90% again above around 3×10^5 cm^{-3}.

Reduced collection efficiency can be mainly attributed to vapor depletion or condensation heat release (Lewis and Hering 2013). The vapor depletion effect rendering reduced activation efficiency, often occurs at higher particle number concentrations, greater than one million particles cm^{-3}. It has been cited that at lower number concentration, the condensational heat release effect prevails vapor depletion in water-based condensation growth systems, and its effect can be reduced by decreasing the diameter of the growth tube (Lewis and Hering 2013).

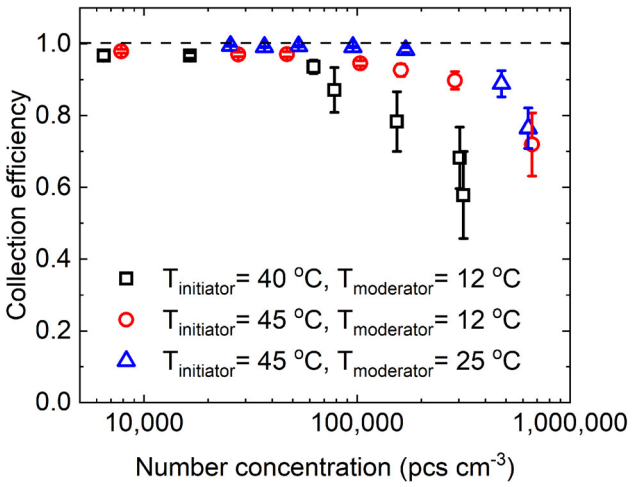

Figure 6. Collection efficiency of the prototype NanoSpot collector as a function of the aerosol number concentration for three different initiator and moderator temperature configurations. 100-nm NaCl test particles were used.

Another option to improve collection efficiency is by increasing the initiator temperature at higher number concentrations. However, higher aerosol concentration also leads to higher aerosol collection rate; thus, in condensation growth collectors where the sample is concentrated on a substrate for analysis, the water evaporation rate on the heated substrate should be much higher than the aerosol collection rate, to avoid water pooling. Finally, an alternate way to mitigate the heat release effect, or water pooling on the collection substrate is by dilution of the aerosol sample at the inlet of the collector.

5.4. Spot sample characteristics: Deposit diameter

Figures 7a–d show SEM micrographs of spot samples for various monodisperse test particles: 20, 100, 700,

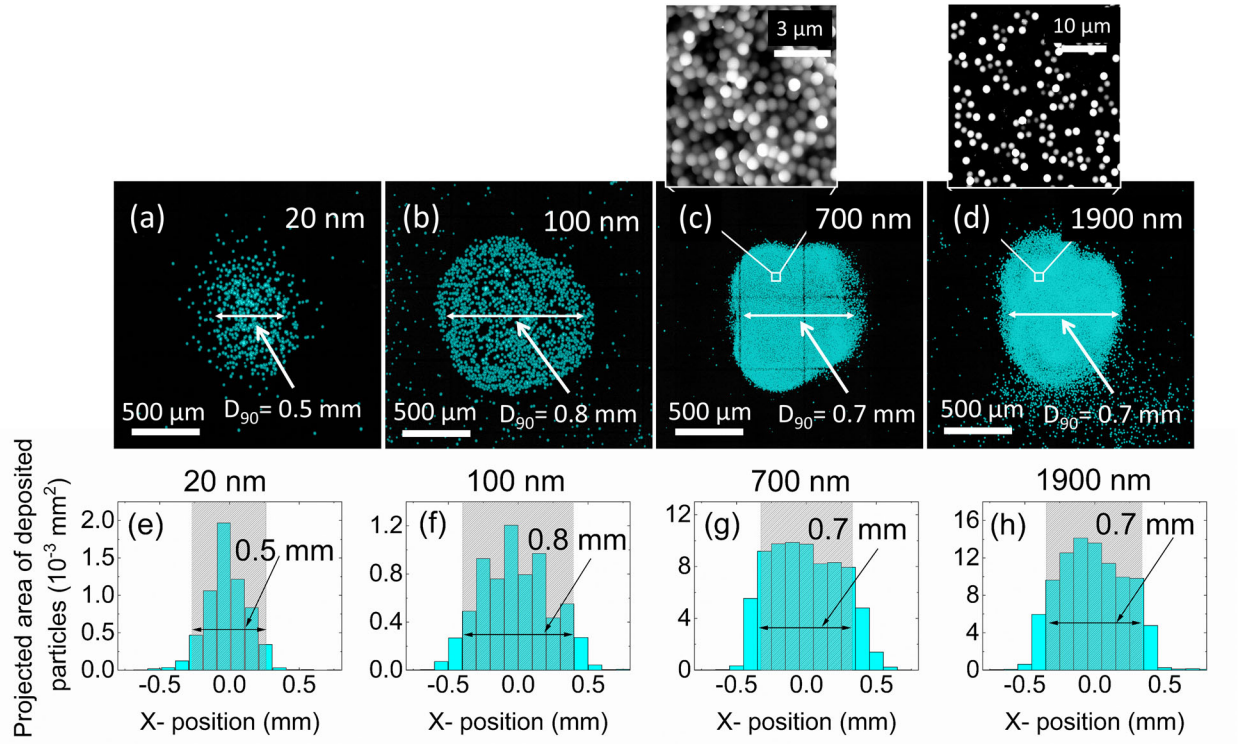

Figure 7. (a-d) SEM images and (e-h) radial distribution of the projected area of the deposited particulate sample of Polystyrene Latex (PSL) particles of 20 nm, 100 nm, 700 nm, and 1900 nm size, when T_{cond}= 5 °C, T_{ini}= 40 °C, and T_{mod}= 12 °C. The shaded area shows width of the distribution corresponding to the diameter of the circle containing 90% of the projected area of the collected particles (D_{90}).

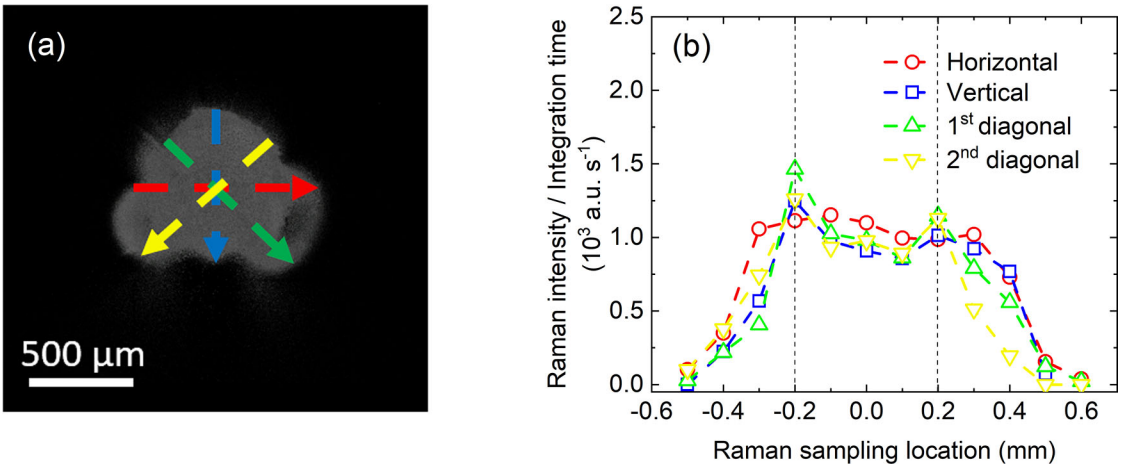

Figure 8. (a) SEM mapped image of silica spot sample with a total particulate mass of 1.3 μg. (b) Raman Intensity signal obtained for spot shown in (a) as a function of the radial location of Raman laser; four different curves corresponding to four different rastering paths shown in (a) were used. The area bound by the dashed lines in (b) has relatively uniform intensity. The edge effects with declining Raman intensity were due to partial sampling of the spot by the laser. The laser spot size at the focal point was estimated to be about 105 µm. The initiator temperature was set at 45 °C.

1900 nm diameter. The initiator temperature was set at 40 °C. The deposition spot images obtained while the initiator temperature was at 45 °C is depicted in Figure S3 in SI. Circular deposition spots were acquired for the smaller particles (20 and 100 nm), while the formation of a "triple lobe shape" deposition was particularly noticeable in the depositions of larger particles (700 and 1900 nm). Smaller droplets, that are expected to be originated from smaller particles, require a longer focal distance than bigger droplets. At a constant nozzle-to-plate distance, where small droplets are merging effectively closer to the centerline, bigger droplets are crossing the central axis before impaction (Hari, McFarland, and Hassan 2007). Large droplets formed in the growth tubes of the NSC, have short focusing distance that is much shorter than the distance to the substrate. Moreover, it appears that the flows emerging from each tube do not mix well enough in the converging nozzle and remain separate laminar flows. The resulting uniformity of the deposit spot was examined and discussed in the next section.

The spatial distribution of the collected particles was acquired and is shown in Figures 7e–h. The diameter of the area, within which ninety percent of the projected area of the collected particles is located, is termed as D_{90}, and is used as the measure of the spot diameter. The spot diameter of 20–1900 nm diameter particles was between 0.5 and 0.8 mm. This diameter was independent of the particle size; an average spot diameter of about 0.7 mm was estimated.

5.5. Spot sample characteristics: Deposit uniformity

The spatial uniformity of the collected particle sample through the NSC was examined by employing Raman Spectroscopy. Specifically, deposit uniformity across the "triple lobe shape" spot sample was assessed. The Raman intensity obtained at different sampling locations, across the sample's diameter is shown in Figure 8. For that, crystalline silica (Min-U-Sil@5) was collected on the warmed surface of a SEM stub, that was embodied in the NSC. The initiator temperature was set at 45 °C. The particulate mass of the collected sample was approximately 1.3 μg. Stepwise spectra were acquired every 0.1 mm across four different "paths" on the collected sample (horizontal, vertical, and two diagonal; Figure S4 in SI), presented in Figure 8a, starting from the edge of the sample, scanning across the sample's diameter until the opposite edge.

The Raman intensities obtained, for the four different sampling "paths," as a function of the sampling locations are shown in Figure 8b. Near the edge of the collected sample, the Raman intensity is negligible, while as the sampling location approaches the deposit spot center, the Raman signal increases, until it finally reaches a plateau, around the spot center. Then, as the sampling location moves further from the sample center, the intensity starts decreasing again until it approaches near-zero values, at the edge of the sample. Moreover, a slight increase of the Raman intensity is observed at the beginning and the end of the plateau, probably due to accumulation of mass from the overlapping of the "three lobes," formed from the overfocusing of the large droplets, following the merging of the droplet-laden stream exiting the triple growth tube of the NSC. The Raman intensity signal remains relatively constant for all paths, in an annular area around the center of the collected sample, with a diameter of

approximately 0.4 mm (the area within the dashed lines shown in Figure 8b). Thus, it is recommended that optical spectroscopy intensities are to be obtained in the specified area, for more uniform data.

5.6. Calibration for Raman measurement

Several Raman spectra were acquired for different crystalline silica mass collected through the NSC (Figure S5 in SI). The obtained Raman intensity per unit time was plotted as a function of the particulate mass per unit area in Figure 9 (Raman intensity per unit time as a function of the particulate mass is presented in Figure S6 in SI). Two calibration curves were extracted from the linear fit curves obtained from the experimental data, for two different initiator temperatures, 40 and 45 °C. The trendline equation derived from the calibration curves, is shown:

$$\frac{I_p}{t} = S^* \frac{m_p}{A_d} \tag{17}$$

where I_p is the Raman Intensity signal, t is the Raman integration time (s), m_p is the particulate mass collected (μg), A_d is the deposition area (mm^2) and S^* is the slope of the calibration curve. The Raman signal intensities were obtained in the recommended area within a radius of 0.2 mm around the spot center.

It was observed that the uncertainty of the normalized Raman signal was higher at the lowest initiator temperature (40 °C) tested, particularly at higher mass loadings, indicating relatively higher nonuniformity in the spot sample. Additionally, the slope of the calibration curve is smaller when the initiator temperature is set at 40 °C. The slopes of the calibration curves ($S^*_{40°C} = 172.6\ mm^2\ \mu g^{-1}$, $S^*_{45°C} = 277\ mm^2\ \mu g^{-1}$) are an indicator of the analytical measurement sensitivity. At initiator temperature of 45 °C, the measurement sensitivity is approximately 1.6 times higher than that at initiator temperature of 40 °C. Since the deposition area diameter and the collection efficiency attained at both initiator temperatures were approximately similar, the differences observed in Figure 9 could most likely be attributed to higher spatial mass density of the spot sample at higher initiator temperature, which in turn was likely due to higher growth efficiency and collection. Based on the aerosolized crystalline silica's size distribution used for collection (Figure S7 in SI), the highest number concentration was measured for particles with the aerodynamic diameter around 500 nm. At this particle size the droplets that are to be formed are not expected to be big enough to cause overfocusing of the droplet-laden stream, as we mainly see for particle with sizes of 700 nm or 1900 nm (Figure 7). Thus, the droplets that are expected to be generated throughout the triple growth tube when the initiator temperature is higher (T_{ini} = 45 °C) are to be deposited closer to the central axis, instead of further away from the center. However, at any particle size distribution, the higher initiator temperature (T_{ini} =45 °C) is anticipated to render better collection. Therefore, higher initiator temperatures above 45 °C are recommended.

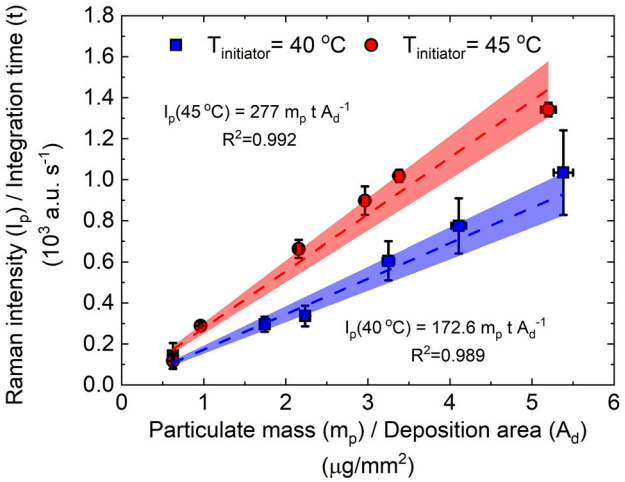

Figure 9. Calibration curves extracted for Raman Intensity per unit time as a function of the particulate mass per unit area for crystalline silica particles. The y-error bars represent the standard deviation of the three Raman intensity replicates obtained at the center of the spot sample. The x-error bars represent the uncertainty of the particulate mass per unit of deposition area of spot sample. The dashed lines represent the linear fit of the experimental data. The shaded area represents the 95% confidence limits around the regression line.

5.7. Analytical measurement sensitivity

Through the NSC, attainment of nearly complete and size-independent sample collection, on a miniscule deposition area, was successfully verified, enhancing the intensity signal from optically spectroscopic analysis. Nevertheless, further comparison of the NSC was accomplished with prevalent particle collection techniques, such as the Sequential Spot Sampler, aerosol focusing and collection through the implementation of aerodynamic lenses and the conventional technique of air filtration.

The calibration curve's slope (S^*) obtained from Figure 9, can serve as the Raman spectroscopic analysis sensitivity. By assuming that the aerosol of interest and the analysis conditions remain identical when implementing different collection techniques and by using the measured sensitivity, the analytical measurement sensitivities of prevalent particle collection methods can

Table 1. Operating parameters of aerosol collection techniques for calculation of the analytical measurement sensitivity for spectroscopic analysis and the estimated uncertainty using Poisson counting statistics for phase contrast microscopy.

Collection technique	Collection efficiency	Aerosol sample flow rate (L min^{-1})	Spot sample diameter (mm)
NanoSpot™ collector	0.9	1.2	0.7
Sequential Spot Sampler™	0.95	1.5	1.0
Aerodynamic lenses[a]	0.3–1.0	0.108	0.37–22.67
13-mm-filter	1.0	2	13
25-mm-filter	1.0	2	25

[a]The Aerodynamic Lens Systems Calculator (Wang and McMurry 2006a, 2006b) was implemented for the aerodynamic lens developed by Liu et al. (1995).
[b]The sample collection time used for the analytical measurement sensitivity calculations was 1 min.

be extracted and then be compared with the measurement sensitivity of the NSC.

The nominal particulate mass (m_p; μg) that is expected to be collected for subsequent spectroscopic analysis was calculated:

$$m_p = \eta_c \; Q \; C_{in} \; t_c \tag{18}$$

where the size-dependent collection efficiency of each of the collection technique applied is denoted by η_c, the aerosol-laden stream flowrate is denoted by Q (L min^{-1}), the aerosol mass concentration is denoted by C_{in} ($\mu g\ m^{-3}$), and the collection time is denoted by t_c (min). From Equations (17) and (18), the following equation can be derived:

$$\frac{I_p}{t} = \frac{S^* \eta_c \; Q \; t_c}{A_d} \; C_{in} \tag{19}$$

By plotting the Raman signal intensity per unit integration time (I_P/t; a.u. s^{-1}) as a function of the aerosol mass concentration (C_{in}; $\mu g\ m^{-3}$), the slope corresponds to the constant of $S^* \eta_c \; Q \; t_c / A_d$. This constant represents the analytical measurement sensitivity (S_c; $mg^{-1}m^3$):

$$S_c = \frac{S^* \eta_c \; Q \; t_c}{A_d} \tag{20}$$

Equation (20) can then be implemented for calculating the analytical measurement sensitivity of the NSC, Sequential Spot Sampler, the Aerodynamic Lenses, and the filtration. Table 1 shows the operating parameters of the NSC, the Sequential Spot Sampler, the Aerodynamic Lenses apparatus, and the filtration used for the calculation.

The analytical measurement sensitivities are shown in Figure 10. NSC spot samples showed the highest measurement sensitivity; approximately 778 $mg^{-1}m^3$. 13-mm and 25-mm diameter filter collection had the lowest sensitivity at 4 $mg^{-1}m^3$ and 1 $mg^{-1}m^3$, respectively. The measurement sensitivity of the NSC was approximately two orders of magnitude higher than that of the filter. The measurement sensitivity for the aerodynamic lenses was found to be size dependent, peaking at approximately 276 $mg^{-1}m^3$ for particles with a diameter of 800 nm. An analytical sensitivity of the Sequential Spot Sampler was 320 $mg^{-1}m^3$, approximately 2.4 times lower than the NSC. NSC had the highest analytical measurement sensitivity.

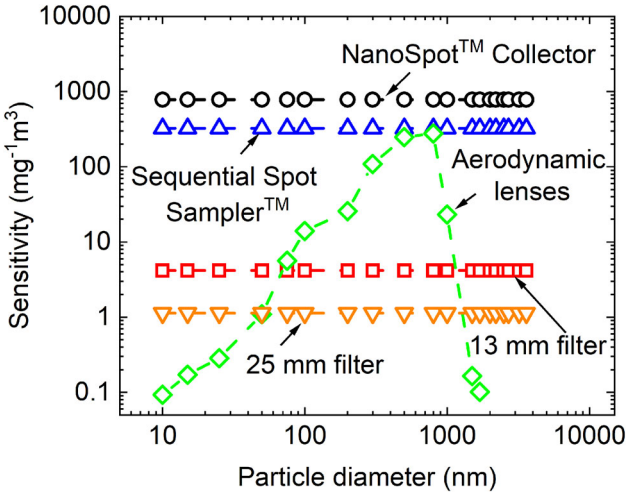

Figure 10. (a) Analytical measurement sensitivity promoted by different particle collection techniques as a function of the particle diameter for direct-on-substrate Raman analysis. NSC provides the highest sensitivity, followed by the Sequential Spot Sampler (lower by a factor of 2.4). The sensitivity from ADL is size dependent and is overall low due to lower sampling flow rate. Total filter collection provides the least sensitivity.

5.8. Poisson counting statistics of fiber concentration measurement

Calculations were performed to compare Poisson counting statistics of fiber concentration measurement using the phase contrast microscopy (PCM; NIOSH Method 7400) for various collection methods. The uncertainty (σ%) of the PCM fiber counting method can be calculated:

$$\sigma \; = \frac{1}{\sqrt{N}} \tag{21}$$

where N is the total number of fibers in the microscopy analysis area. The estimated sample collection time (t_c) needed to achieve target counting uncertainty for measurement of 0.1 fiber/cm^3 (C_f) using the NIOSH Method 7400 for various collection methods was calculated and is shown in Figure 11:

$$t_c = \frac{N \; A_d}{A_m \; C_f \; Q \; \eta_c} \tag{22}$$

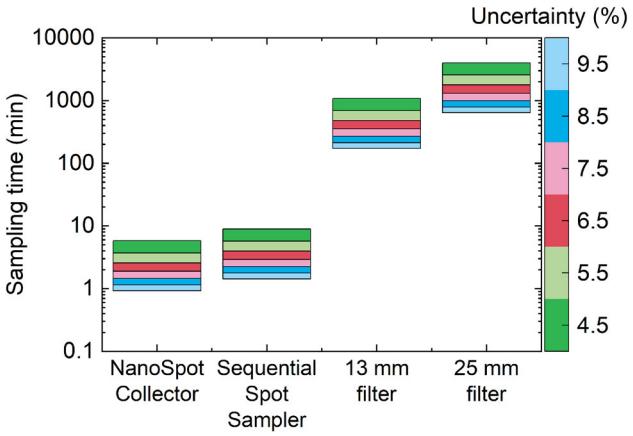

Figure 11. Comparison of estimated uncertainty using Poisson counting statistics for phase contrast microscopy analysis (NIOSH Method 7400) for fiber air concentration measurement using various collection methods. Y-axis shows sample collection time needed for various methods to achieve a certain target counting uncertainty (shown by graded color scale) of fiber number concentration measurement. The fiber air concentration of 0.1 fibers cm^{-3} was assumed. The NIOSH Method 7400 recommends that the fiber density on the substrate be in the range of 260–1300 mm^{-2} (for a substrate area for microscopy analysis of 0.385 mm^2) for optimum and unbiased counting. Excellent counting statistics can be obtained with NSC with short collection times that are two to three orders of magnitude better than the conventional filter collection methods.

where A_d is the spot deposit area of each collection technique and A_m is the microscopy analysis area. The recommended substrate area for microscopy analysis is 0.785 mm^2 (NIOSH 2019). The area of the spot sample from NSC was about 0.385 mm^2, whereas the area over which the sample was collected using the 13 mm and 25 mm filters was 133 and 491 mm^2 respectively. For a substrate area for microscopy analysis of 0.385 mm^2 (A_m), a fiber density on the substrate in the range of 260–1300 mm^{-2} is recommended for optimum and unbiased counting ($\sigma = 4.5$–10%). For the NSC the entire spot sample can be used for PCM analysis, whereas only a fraction of filter sample is used.

Sample collection time, to achieve a certain target counting uncertainty (4.5–10%), was two to three orders of magnitude better for NSC (and Sequential Spot Sampler), compared to the filter collection methods. To achieve a 10% counting uncertainty, the NSC needed only 0.93 min collection time whereas, the 13 mm filter and the 25 mm filter needed 172 min and 637 min, respectively.

6. Conclusions

The design and characterization of a new, compact portable particle collector, the "NanoSpot Collector," was described. Good collection efficiency was obtained for aerosol particles, down to 7 nm in diameter, for water-soluble and insoluble particles. Moreover, the collection efficiency was greater than 90% for number concentrations of approximately up to 3×10^5 cm^{-3}. Relatively uniform deposition spots were acquired for particles in the diameter range of 20–1900 nm, with a particle size-independent deposition spot diameter of approximately 0.7 mm. Larger particles, above 700 nm, produced triple-lobe-shaped spots as a result of higher inertial during focusing downstream of the exit nozzle prior to impaction. Additionally, the spot deposit was examined through Raman spectroscopy and was found to be relatively uniform within a spot diameter of approximately 0.4 mm. Raman spectroscopy was also used for the extraction of mass calibration curves. Higher initiator temperature was found to significantly enhance the analytical measurement sensitivity; when the initiator temperature was increased from 40 to 45 °C, the sensitivity improved by 60%. Higher temperature also produces more uniformity as shown by the reduced uncertainty of the calibration curve. Moreover, the measurement sensitivity provided by the NanoSpot collector was compared with other conventional collection techniques, such as the Sequential Spot Sampler, the aerosol collection through the implementation of aerodynamic lenses and the prevalent collection technique of filtration. NanoSpot collector exhibited the highest collection sensitivity; 2.4 times higher than that of the Sequential Spot Sampler, and two orders of magnitude greater than that of the 13- and 25-mm-diameter filter collection. For fiber counting applications using phase contrast microscopy, spot samples provided two to three orders of improvement in collection time (to achieve the same target uncertainty) or counting uncertainty (for the same collection time). The study demonstrates that the NanoSpot collector can be used for qualitative and quantitative microscopy and spectroscopy applications with high analytical sensitivity and low counting uncertainty.

Acknowledgments

The authors would like to thank Dr. Chaolong Qi for his valuable feedback on this manuscript.

Disclosure statement

The findings and conclusions in this report are those of the author(s) and do not necessarily represent the official position of the National Institute for Occupational Safety and Health, Centers for Disease Control and Prevention.

ORCID

Orthodoxia Zervaki http://orcid.org/0000-0002-3481-506X
Dionysios D. Dionysiou http://orcid.org/0000-0002-6974-9197
Pramod Kulkarni http://orcid.org/0000-0001-7692-4662

References

Aitken, J. 1888. On the number of dust particles in the atmosphere. *Nature (London)* 37 (957):428–30.

Allen, M. D., and O. G. Raabe. 1982. Re-evaluation of Millikan's oil drop data for the motion of small particles in air. *J. Aerosol Sci.* 13 (6):537–47.

Bird, R. B., W. E. Stewart, and E. N. Lightfoot. 2007. *Transport phenomena*. Rev. 2nd ed., 928. New York: Wiley.

Brockmann, J. E. 2011. Aerosol transport in sampling lines and inlets. In *Aerosol measurement: Principles, techniques, and applications*, ed. P. Kulkarni, P. A. Baron, and K. Willeke, 3rd ed., 69–105. New Jersey: Wiley.

Clift, R., J. R. Grace, and M. E. Weber. 1978. *Bubbles, drops and particles*. 3rd ed. New York: Academic Press.

Davies, C. N. 1945. Definitive equations for the fluid resistance of spheres. *Proc. Phys. Soc.* 57 (4):259–70.

Eiguren Fernandez, A., G. S. Lewis, and S. V. Hering. 2014. Design and laboratory evaluation of a sequential spot sampler for time-resolved measurement of airborne particle composition. *Aerosol Sci. Technol.* 48 (6):655–63.

Hari, S., A. R. McFarland, and Y. A. Hassan. 2007. CFD study on the effects of the large particle crossing trajectory phenomenon on virtual impactor performance. *Aerosol Sci. Technol.* 41 (11):1040–8.

Hering, S. V., G. S. Lewis, S. R. Spielman, and A. Eiguren-Fernandez. 2019. A MAGIC concept for self-sustained, water-based, ultrafine particle counting. *Aerosol Sci. Technol.* 53 (1):63–72.

Hering, S. V., S. R. Spielman, and G. S. Lewis. 2014. Moderated, water-based, condensational particle growth in a laminar flow. *Aerosol Sci. Technol.* 48 (4):401–8.

Hinds, W. C. 1999. *Aerosol technology: Properties, behavior, and measurement of airborne particles*. 2nd ed. New York: Wiley.

Lewis, G. S., and S. V. Hering. 2013. Minimizing concentration effects in water-based, laminar-flow condensation particle counters. *Aerosol Sci. Technol.* 47 (6):645–54.

Liu, P., P. J. Ziemann, D. B. Kittelson, and P. H. McMurry. 1995. Generating particle beams of controlled dimensions and divergence: II. Experimental evaluation of particle motion in aerodynamic lenses and nozzle expansions. *Aerosol Sci. Technol.* 22 (3):314–24.

[NIOSH] National Institute for Occupational Safety and Health. 2019. Method 7400. In *NIOSH Manual of analytical methods, Asbestos and other fibers by PCM*, 5th ed. Cincinnati, OH: U.S. Department of Health and Human Services, Centers for Disease Control and Prevention, National Institute for Occupational Safety and Health.

Raynor, P. C., D. Leith, K. W. Lee, and R. Mukund. 2011. Sampling and analysis using filters. In *Aerosol measurement: Principles, techniques, and applications*, ed. P. Kulkarni, P. A. Baron, and K. Willeke, 3rd ed., 107–28. New Jersey: Wiley.

Schneider, C. A., W. S. Rasband, and K. W. Eliceiri. 2012. NIH image to ImageJ: 25 years of image analysis. *Nat. Methods.* 9 (7):671–5.

Seinfeld, J. H., and S. N. Pandis. 2012. Cloud physics. In *Atmospheric chemistry and physics: From air pollution to climate change*, 2nd ed., 1333. New Jersey: Wiley.

Wang, X., and P. H. McMurry. 2006a. A design tool for aerodynamic lens systems. *Aerosol Sci. Technol.* 40 (5): 320–34.

Wang, X., and P. H. McMurry. 2006b. Instruction manual for the aerodynamic lens calculator. *Aerosol Sci. Technol.* 40 (5):1–10.

Wei, S., B. Johnson, M. Breitenstein, L. Zheng, J. Snawder, and P. Kulkarni. 2022. Aerosol analysis using handheld Raman spectrometer: On-site quantification of trace crystalline silica in workplace atmospheres. *Ann. Work Exposures Health* 66 (5) :656–70.

Wei, S., P. Kulkarni, K. Ashley, and L. Zheng. 2017. Measurement of crystalline silica aerosol using quantum cascade laser-based infrared spectroscopy. *Sci. Rep.* 7 (1):13860.

Wei, S., P. Kulkarni, L. Zheng, and K. Ashley. 2020. Aerosol analysis using quantum cascade laser infrared spectroscopy: Application to crystalline silica measurement. *J. Aerosol Sci.* 150:105643.

Zheng, L., P. Kulkarni, M. E. Birch, K. Ashley, and S. Wei. 2018. Analysis of crystalline silica aerosol using portable Raman spectrometry: Feasibility of near real-time measurement. *Anal. Chem.* 90 (10):6229–39.